Development and experimental performance of micro-CSP heliostat controllers under IEC 62817 criteria

Esteban López, *Jordan* Pacheco, and *William* Oñate*

Universidad Politécnica Salesiana (UPS), Electronics and Automation Department,Quito 170146, Ecuador

Abstract. Control strategies in CSP plants mitigate the effects of solar variability, optimize resource use, and reduce CO2 emissions. However, most studies address solar movement tracking using advanced controllers and rely on dynamic simulation models that, while useful for exploring certain scenarios, often idealize operating conditions and oversimplify the effects of external loads. This work presents the implementation of a micro-CSP system with three heliostats developed for this study, which serves as an experimental platform to contribute to the validation of the performance of three control strategies: proportional-integral—derivative (PID), fuzzy logic (FLC), and perturb/observe angular tracking (P&O-AT), considering metrics such as energy consumption, accuracy, and thermal performance. The performance evaluation of the controllers under certain external load conditions specified in IEC 62817 for CSP systems reveals significant differences in their operability. The PID controller demonstrated superior efficiency in balancing energy consumption, accuracy, and thermal performance. On the other hand, the FLC stood out for its response speed, achieving a shorter settling time against disturbances, albeit at the cost of a higher computational load. In contrast, the P&O-AT algorithm exhibited the lowest CPU usage but lower focal accuracy and longer response times to the target point.

1 Introduction

Environmental transformation, aligned with global commitments to achieve a sustainable energy matrix, has become crucial to counter the anticipated impacts of climate change. This situation emphasizes solar energy as a renewable resource, which is being researched on two technological fronts: photovoltaic (PV) systems and concentrating solar power (CSP) systems. Concentrating solar power systems focus solar radiation using mirrors or lenses onto a target point to generate high temperatures, which are then converted into electricity. They are classified into two optical groups: linear and point focus. For their operation, these systems require an active solar tracking system with one or two axes, depending on their application, mechanical architecture, and drive [1]. This makes them a promising option for

* Corresponding author: wonate@ups.edu.ec

electricity generation, especially in areas with high levels of solar radiation. Given this background, according to [2], Ecuador receives a global horizontal irradiance (GHI) exceeding 3.8 kWh/m²/day, indicating its potential for implementation and strengthening its future energy matrix.se academic titles.

It is worth noting that the performance of a CSP plant depends not only on the optical subsystem but also on factors such as heat transfer, reflective surfaces, and overall thermal efficiency [3, 4]. In this context, environmental conditions, specifically wind, lead to a relative increase in convective thermal losses [4]. Additionally, significant advances have been made in control algorithms for active solar tracking systems (ASTS) [5, 6]. The literature presents a wide variety of classical and modern algorithms implemented in CSP systems, such as Proportional-Integral-Derivative (PID) control, Fuzzy Logic Control (FLC), and Perturb and Observe (P&O-AT), and even incorporates machine learning strategies to optimize pointing accuracy [7, 8].

Furthermore, [9, 10] demonstrates that the adoption of predictive and adaptive control strategies entails integrating real-time monitoring systems with high-sampling-frequency capabilities and distributed computing architectures to process large volumes of thermal and heliostat position data.

Similarly, [11] highlights that advanced controllers based on neural networks and machine learning techniques require a low-latency communication network, a calibration process supported by sensing, and a robust infrastructure of sensors and actuators in order to achieve accurate responses. From the above, it is evident that there is limited contrast in the ability to identify more suitable alternatives in small-scale applications, such as laboratory experimental scenarios. On the other hand, these approaches exhibit bias due to the absence of common scenarios and equivalent testing or simulation conditions, which largely prevents the establishment of universal criteria [12].

Based on the above, this work contributes to the performance evaluation of ASTS control systems implemented in an experimental laboratory micro-CSP. For this purpose, focal-pointing heliostat structures, a local wireless communication architecture, sensor-actuator electronics, and classical and modern control strategies such as PID, Perturb and Observe Angular Tracking (P&O-AT), and fuzzy logic (FLC) were designed. The control algorithms are executed on a local server, and error corrections are sent to the interface modules of each heliostat, thereby enabling performance analysis under the same external load conditions. The validation of the algorithms is based on an experimental performance analysis concerning control criteria (hysteresis, disturbance response, stability, tracking, and oscillations), operational criteria (control system consumption, receiver temperature, cost, constructive complexity, and maintenance), and external loads.

This document is structured as follows: introduction in Section 1, methodology in Section 2, analysis and results in Section 3, discussion in Section 4, and finally, conclusions in Section 5.

2 Materials and methods

To evaluate the CSP's thermal performance, the control systems' performance metrics and the computational expenditure of the control units are considered. For this, it is necessary to develop an array of heliostats integrated with different classical and modern automatic control systems (PID, P&O-AT, and FLC). Their objective is to control the azimuth and elevation angles to reflect global radiation toward a target point, thereby recording thermal concentration using a set of resistance temperature detectors (RTD). In this case study, wind is considered an external load factor that affects the precision and stability of the structures during solar reflection onto a target point in this regard, the IEC 62817 standard is used as a technical reference for evaluating the performance of the solar tracking system based on mechanical, functional, and operational criteria, such as accuracy, motion repeatability, structural deflection, and mechanical oscillations; this framework enables experimental comparison under equivalent operating conditions. Figure 1 shows an experimental micro-CSP with 3 equidistant heliostats placed linearly, where each is composed of remote interface agents (ESP32) that interact with three measurement devices (GPS, MPU6050, and AS5600), two actuation devices (permanent magnet DC motors), and a local server that executes control algorithms on a wireless network with a star topology. In this way, end-to-end interoperability is achieved among the different heterogeneous devices that make up the designed architecture.

On the other hand, each target point has a peripheral interface that outputs to the local server for recording.

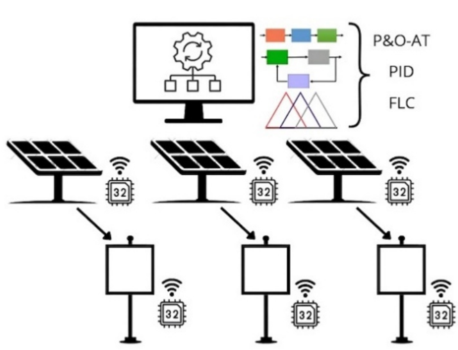

Fig. 1. General scheme of the micro-CSP.

For a specific explanation of the CSP operation stages, this section is structured into 4 subsections that provide an orderly approach to both the technical and functional aspects of the system. The first section covers the development of the rotational support (azimuth and elevation angles); the second presents the electronic adaptation process for automatic solar tracking; the third describes the design of a centralized wireless communication network between the local server and the ESP32s; and the final subsection develops the control strategies.

2.1 Support structure in ASTS

Due to their operational analogy, each structure has a mechatronic design used in PV systems. Three dual-axis solar tracking heads from the Well&J. Technology [6] brand were acquired; their technical characteristics are shown in Table 1.

Table 1. Specifications of the dual-axis DC head for solar tracking.

Characteristics	Technical Specifications
Material	Aluminum
Supply Voltage	24 V DC (max 4 kg) /12 V DC (max 2,5 kg)
Safety	Limit switches
Speed	1revolution/minute
Azimuth Range	0°-350°
Elevation Range	0°-170°

This design consists of two rotational aluminum bases: in the azimuth plane, a displacement range of 0° to 180° was established, and in the elevation plane, a displacement range of 0° to 90° was defined. Two DC gearmotors control the rotation of the planes based on load and speed, generating the necessary torque for the structure's angular positioning, as shown in Figure 2.

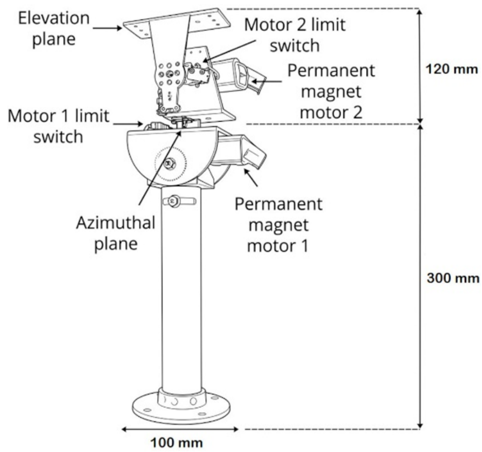

Fig. 2. Schematic and dimensions of the dual-axis DC head.

In line with the criteria considered in IEC 62817 standard, the performance of the tracking structure depends not only on angular displacement but also on its mechanical stability under external loads

In Figure 2, a dimensioned scheme of the ASTS is observed, where the azimuth base supports the elevation plane and on which a wooden base of 500mm x 500mm was placed, adhered with a sheet having reflectivity index characteristics of 80% to 90%, thermal insulation of 80% to 100%, and transmittance of 10% to 20%. With the azimuth plane parallel to the ground and an elevation angle of 170°, the structure reaches a maximum height of 420mm.

2.2 Electronic adaptation in ASTS

To more accurately capture angular changes during solar tracking, several electronic sensor adaptations were implemented in the azimuth and elevation planes, including a gyroscope and a magnetic encoder. The AS5600 Hall-effect encoder sensor is an absolute angular sensor that detects azimuth movement via the reference magnetic displacement. The MPU6050 gyroscope senses the inclination of the elevation plane to angular position values. The reading from these two sensors is transmitted to the interface agent via the I²C protocol.

To know the geographical coordinates of each ASTS, a Ublox Neo-6M-V2 GPS module and the Data Time library in C++ were integrated; in this way, the theoretical position of the sun in real-time, called the solar vector, is calculated, which is also transmitted to the interface agent via the UART protocol, as observed in Figure 3.

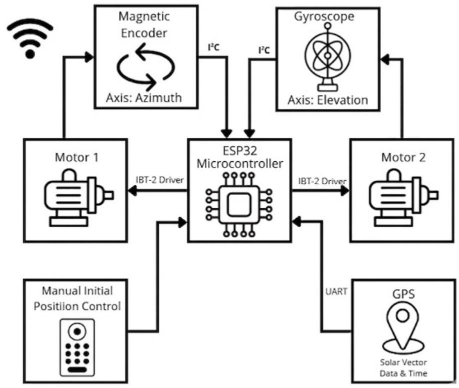

Fig. 3. Block diagram of the electronic integration in the solar tracker head.

2.3 Communication network in a heliostat array

To ensure coordination and real-time control from the operations base to the three heliostats, an IEEE 802.11n (2.4 GHz) Wi-Fi wireless communication network was implemented, connecting the interface modules (ESP32-Wrover nodes) in a star topology and using the WebSocket protocol. The data structure includes unique node identification, useful information (azimuth and elevation plane angular positions, geographical position, and control algorithm correction commands), and a verification field. In this way, a local Full-Duplex access point is available for data transmission and reception, with a 1-second sampling interval to avoid communication saturation. Figure 4 shows the topology diagram of the wireless communication network between the local server and the heliostats.

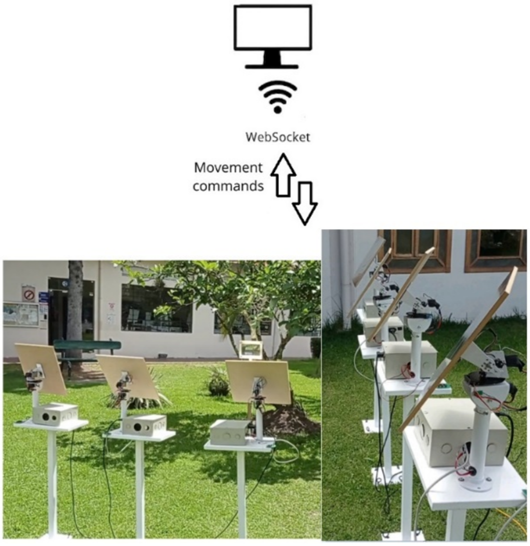

Fig. 4. Server/client wireless network topology for heliostats with ESP32.

2.4 Control strategies implemented in CSP

To achieve a global balance in the performance of the control systems, three different algorithms were implemented: one open-loop (P&O-AT) and two closed-loop (PID and FLC), which, in a certain way, share similarities in driving the system to a desired state based on the error.

From the local server, certain georeferencing vectors are received, enabling continuous calculation of the setpoint (see Eq. 1). In this way, the parameters are adjusted according to operating conditions. This correction process adapts over time, and as a result, a vector normal to the rotating support's plane is obtained at each instant.

$$\mathbf{N}\rightarrow = (\mathbf{S}\rightarrow + \mathbf{T}\rightarrow) / (\| \mathbf{S}\rightarrow + \mathbf{T}\rightarrow \|) \tag{1}$$

In the case of the elevation angle, seasonal variations in solar height are reflected, caused by the Earth's translation and the tilt of its axis, where S is the solar vector (from the heliostat to the sun), and T is the target vector (from the heliostat to the target point).

Meanwhile, the azimuth angle changes as a function of time and is calculated using spherical trigonometry (see Eq. 2) [9], where φ is the latitude, δ the solar declination, t the solar time, h the solar altitude, dAz/dt the variation of azimuth with respect to time, and w is the Earth's angular rotation speed of 15°/hour [9].

$$dAz / dt = \cos(h) / [\omega \cos(\delta)] \tag{2}$$

The geographic coordinates provided by the GPS module and Coordinated Universal Time (UTC-5) allow the ASTS to have coordinated movement for tracking.

2.4.1 PID Controller

The direction of the bisector is obtained from the division point between the adjacent sides (solar and target vectors), and its deviation serves as the feedback error for the controller (see Figure 5). This discretized value is used to weight the correction gains as follows: the proportional gain acts directly on this instantaneous value, producing a signal whose magnitude is proportional to the error deviation; the integral gain accumulates the error over time from the proportional value that failed to eliminate it, as long as a difference exists between the process variable and the reference; the derivative gain evaluates how quickly the error varies, anticipating the error trend or providing a preventive correction.

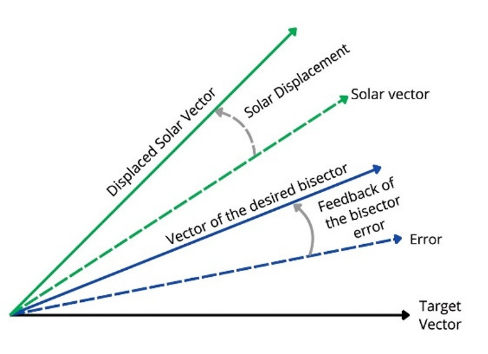

Fig. 5. Representation of sun-target orientation for error calculation.

Although Figure 6 (a) presents a single diagram of the control system, in practice, two distinct regulation architectures were implemented: one for the azimuth axis and another for the elevation axis. Each controller operates independently to ensure the autonomy of the degrees of freedom associated with its respective axis, and both are executed on the local server via a Python script. In the case of the azimuth PID controller, a local East-North-Up (ENU) coordinate system is used. This system defines the direction of the bisector vector in space and allows for correction of the eastward movement, which is opposite to the natural path of the sun. This setpoint is updated at the instant the target vector is fixed (see Figure 6 (b)). For the elevation PID controller, the direction of the bisector vector is corrected during the horizontal movement of the heliostat's inclined plane with respect to ENU. This setpoint is also updated when the target vector is fixed (Figure 6 (c)).

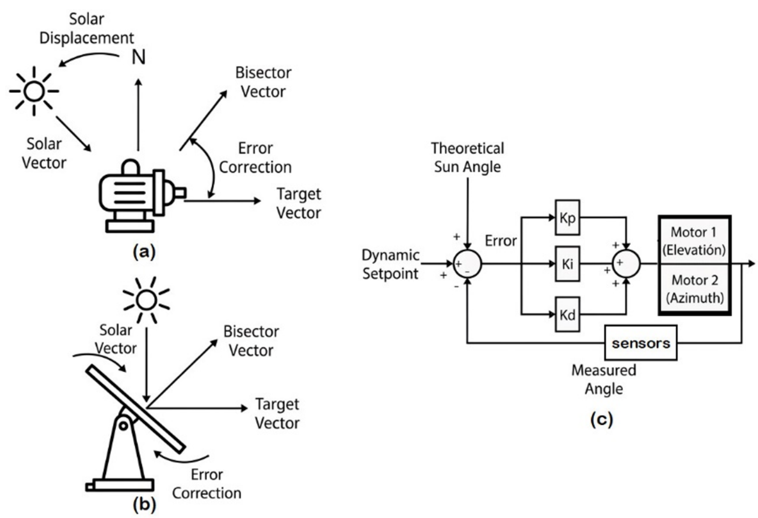

Fig. 6. (a) Simplified scheme of PID controllers ((b) azimuth and (c) elevation).

To adjust the proportional (Kp), integral (Ki), and derivative (Kd) gain parameters, the black-box method was chosen, using GPS, gyroscope, and magnetic encoder data as inputs and outputs. This approach yielded a second-order transfer function that enables measurement of the controlled variable for each axis and the correction signals sent to the actuators. Table 2 lists the gains and models of the PID controllers for azimuth and elevation. The controlled variable (CV) is defined as the tracking angle, and the manipulated variable (MV) as the movement commands.

Table 2. Parameters and variables of the control loop.

Parameters	CSP PID AZIMUTH	CSP PID ELEVATION
Kp	2	2
Ki	0.1	0.15
Kd	0.5	0.6
f(t)	$\frac{0.598039}{s\,(1.280s+1)}$	$\frac{-0.082042}{s\,(0.576s+1)}$
VC	Real azimuth angle	Real elevation angle
VM	Right/Left correction command	Up/Down correction command
Dynamic disturbance	Solar vector displacement	Solar vector displacement

2.4.2 Fuzzy Logic Controller (FLC)

The controller is based on a set of heuristic rules that define fuzzy partitions of the input space, grouping numerical values into linguistic categories such as "positive large" or "close to zero". From these classifications, a rule base is built for each axis, linking system conditions to specific control actions. Each block receives as inputs the error between the setpoint and the position, as well as its temporal variation. These variables are evaluated using trapezoidal membership functions defined in the universe interval (0,1).

Table 3 presents, for each axis, the inference rules that express relationships of the form: "if the error is small and positive and the variation is negative, then decrease movement".

Table 3. Linguistic inference rules applied to azimuth and elevation axes.

FLD AZIMUTH INFERENCE RULES	FLD ELEVATION INFERENCE RULES
1. If (error is NG) then (output1 is NEG)	1. If (error_azimut is NG) then (u_azimut is NEG)
2. If (error is NP) and (de_error is z) then (output1 is NEG)	2. If (error_azimut is NP) and (de_error_azimut is z) then (u_azimut is NEG)
3. If (error is NP) and (de_error is n) then (output1 is NEG)	3. If (error_azimut is NP) and (de_error_azimut is n) then (u_azimut is NEG)
4. If (error is PG) then (output1 is POS)	4. If (error_azimut is PG) then (u_azimut is POS)
5. If (error is PP) and (de_error is z) then (output1 is POS)	5. If (error_azimut is PP) and (de_error_azimut is z) then (u_azimut is POS)
6. If (error is PP) and (de_error is p) then (output1 is POS)	6. If (error_azimut is PP) and (de_error_azimut is p) then (u_azimut is POS)
7. If (error is ZE) then (output1 is ZERO)	7. If (error_azimut is ZE) then (u_azimut is ZERO)
8. If (error is NP) and (de_error is p) then (output1 is ZERO)	8. If (error_azimut is NP) and (de_error_azimut is p) then (u_azimut is ZERO)
9. If (error is PP) and (de_error is n) then (output1 is ZERO)	9. If (error_azimut is PP) and (de_error_azimut is n) then (u_azimut is ZERO)

The resulting control action is determined using a maximum-activation criterion, which simplifies defuzzification and improves execution speed, as shown in Figure 7. This strategy enables a more agile and consistent response to the system's dynamic variations.

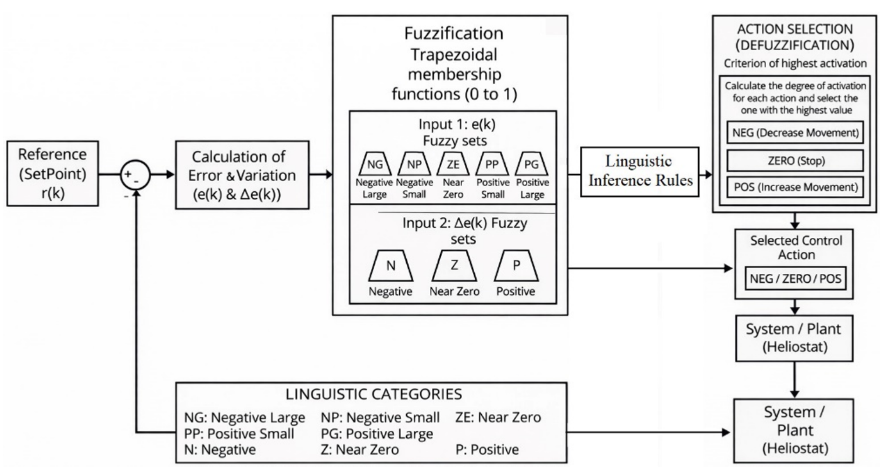

Fig. 7. Scheme of fuzzy control applied to azimuth and elevation axes.

2.4.3 Perturb and Observe Controller – Angular Tracking (P&O-AT)

The P&O-AT control method is based on a practical, direct approach that is simple, versatile, and computationally inexpensive: instead of modeling the system, action is taken on it, and its response is observed; that is, small adjustments are made to the actuator position, and the error in the bisector position is evaluated. For this reason, it is termed P&O-AT angular tracking for this case study.

In this case, as shown in Figure 8, discrete control was applied to the azimuth axis, with adaptive search logic for the inclination of the azimuth plane. The system is perturbed by a displacement error every 4 minutes, simulating the displacement of the solar vector. For the elevation axis, the system stores the last displacement error of the solar vector in memory and compares it with the current error to overwrite the controlled variable.

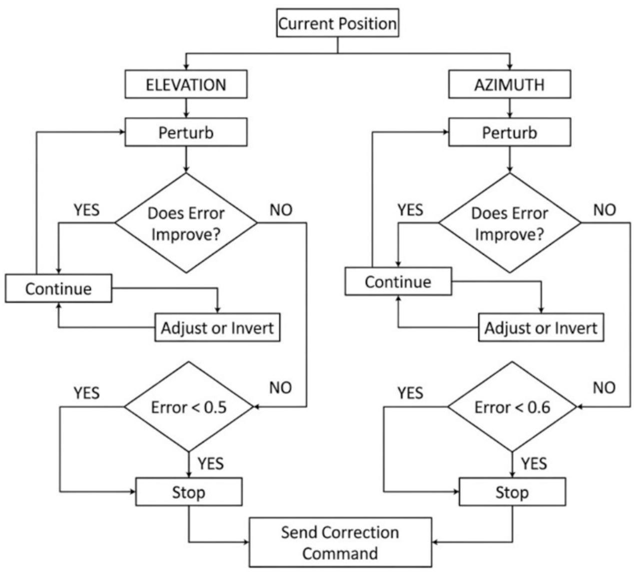

Fig. 8. Scheme of P&O-AT control applied to azimuth and elevation axes.

This controller enforces a 2-second delay between perturbations to prevent hasty corrections and to allow the system to reach a new steady state before evaluating the effect of each change. Additionally, thresholds of 0.5° and 0.6° were set for the elevation and azimuth angles, respectively, in the solar direction, preventing unnecessary movements when the system is sufficiently aligned or close to the bisector vector.

3 Analysis of results

Considering the behavior of the CSP system described in Section 2, the controller performance indicators established were overshoot (OS%), settling time (Ts), and error, which was obtained by comparing the setpoint representing the bisector vector with the solar reference and the current positions of the solar and target vectors. The dynamic disturbance is due to the horizontal displacement of the bisector, not to external disturbances. During experimentation, while recording this data, discrete metrics such as Mean Absolute Error (MAE) and Root Mean Square Error (RMSE) were applied, allowing analysis of deviations from the mean and, in cases of fluctuating transients, as indicated in Table 4.

Table 4. Performance results of control strategies in solar tracking.

Control	Axis	MAE	RMSE	Overshoot %	Settling Time
P&O-AT	Elevation	0.3150	0.3974	1.40	2.6
FLC		0.4716	0.5611	2.03	1
PID		0.3080	0.3920	1.47	1.5
P&O-AT	Azimuth	0.2835	0.3577	2.1	3
FLC		0.3961	0.4713	2.1	1.5
PID		0.2790	0.3520	1.9	2

For the elevation axis, the indicators show consistent differences between strategies in terms of accuracy and dynamics. The PID controller achieves the best overall performance, recording the lowest errors of MAE = 0.3080, RMSE = 0.3920, and a moderate overshoot of 1.47%, with a settling time of 1.5 s, suggesting a stable and adequately damped response. The P&O-AT method presents an accuracy level very close to PID, with MAE = 0.3150, RMSE = 0.3974, and the lowest overshoot (1.40%); however, its settling time increases to 2.6 s, consistent with a more gradual convergence resulting from deliberate perturbations in the search for the optimal point. In contrast, the FLC exhibits the shortest settling time of 1 s, but with greater error dispersion (RMSE = 0.5611) and the highest overshoot (2.03%), indicating more energetic control actions during the transient and a rapid response at the cost of greater variability around the reference.

On the azimuth axis, a similar trend is observed. The PID achieves the best balance between accuracy and stability, with the lowest errors (MAE = 0.2790, RMSE = 0.3520) and the lowest overshoot (1.9%), reaching steady state in 2 s. The P&O-AT maintains comparable accuracy (MAE = 0.2835, RMSE = 0.3577), though with a slower settling time (3 s) and a slightly higher overshoot (2.1%), attributable to the iterative nature of its search strategy. Meanwhile, the FLC reduces settling time to 1.5 s but increases the mean error and its variability (MAE = 0.3961, RMSE = 0.4713) while maintaining a similar overshoot (2.1%), reflecting faster but less precise dynamics.

During the temporal evolution of the system, when it is in a steady state, an external load is applied to the system, revealing the controllers' response in terms of transients, overshoots, and specific errors. For the azimuth axis, a brief mechanical push is applied as an external disturbance to the heliostat structure. However, this action did not induce effective rotation on the azimuth axis, and consequently, there is no error in the CSP system, as observed in Figure 9.

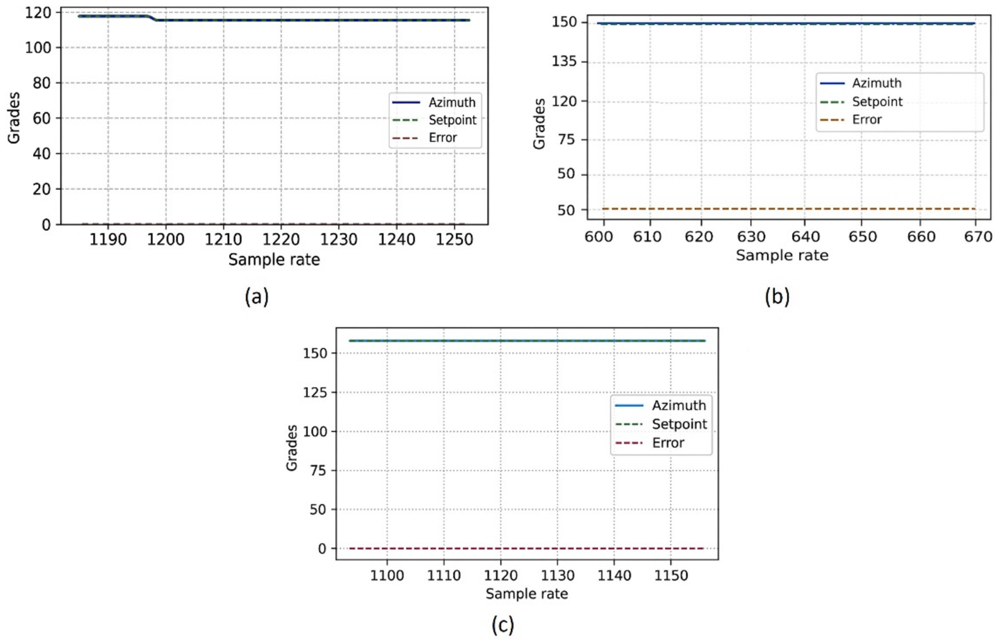

Fig. 9. Temporal responses of the azimuth axis to external disturbances in the controllers (a) FLC, (b) P&O-AT, (c) PID.

Contrary to the above, a momentary misalignment occurred along the elevation axis for all three controllers, demonstrating the control system's ability to correct for a disturbance and the recovery time until the controlled variable is close to zero.

Figure 10 shows the elevation axis control system corresponding to the FLC. The elevation signal, represented by the blue line, remains largely overlaid with the green dotted line (setpoint), even when two external load actions are executed, indicating precise tracking in steady state. The red line shows the transients associated with the system response, during which the variable momentarily deviates from the reference. However, the controller corrects the misalignment and reduces the error to values close to zero within a recovery time of 4.3 seconds, without sustained oscillations, stabilizing around the operating point.

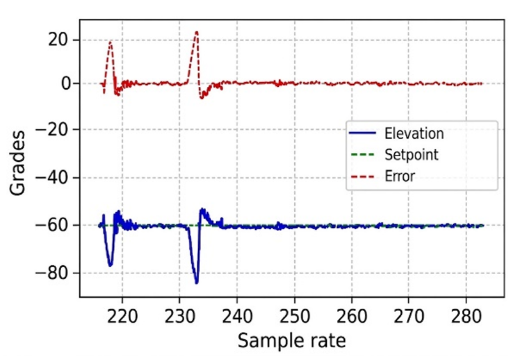

Fig. 10. Temporal responses of the elevation axis to an external disturbance in the FLC controller.

Figure 11 shows the elevation axis control system for P&O-AT. The actual elevation remains close to the bisector setpoint for most of the interval, indicating good tracking around the operating point. However, a slight deviation in the solar direction is maintained to keep the control band stable. When an external load occurs, a more pronounced transient is evident, characterized by deviations in specific peaks and, consequently, an increase in error. Subsequently, the system recovers tracking with small residual fluctuations, and the error returns to values close to zero within an approximate recovery time of 7 seconds, without sustained oscillations.

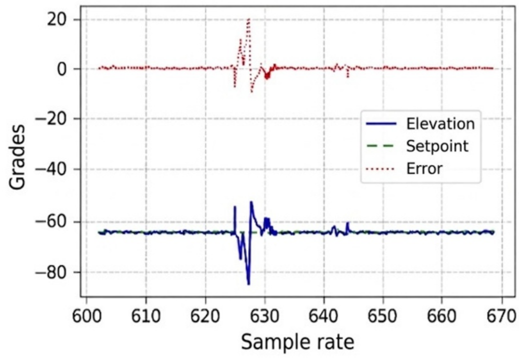

Fig. 11. Temporal responses of the elevation axis to an external disturbance in the P&O-AT controller.

In Figure 12, corresponding to the PID elevation-axis control system, two consecutive transients are observed, associated with additional loads on the heliostat structure. This indicates a momentary misalignment with respect to the bisector vector and, consequently, a corrective movement that brings the error close to zero. Subsequently, the system exhibits a transient with a sign change, resulting from a disturbance applied in the opposite direction, indicating the controller's action to correct and compensate for the error through a damped dynamic without marked oscillations, until the error reaches approximately zero within a recovery time of approximately 5 seconds.

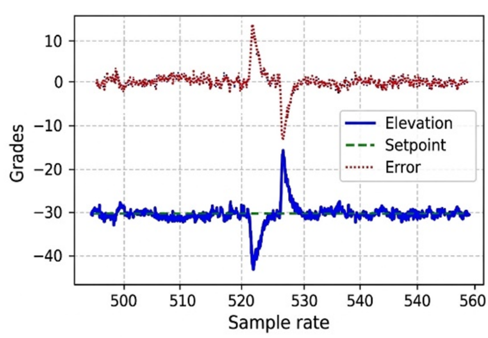

Fig. 12. Temporal responses of the elevation axis to an external disturbance in the PID controller.

Within the performance parameters of the control systems, the computational expenditure of the local server is analyzed. The server has specifications of 20 GB DDR4 RAM, an AMD Ryzen 7 5800H processor with 8 cores and 16 threads, and a processing frequency of 3.2 GHz. Table 5 shows the results of computational expenditure over 240 minutes for the execution of the control algorithm, the discrete transmission of movements, and the reception of angular positions. According to the analysis, the P&O-AT controller drives the processor to an average consumption of 11.43%, the PID controller to an average of 14%, and the FLC controller to an average of 15.46%.

Table 5. Computational load metrics of the controller algorithms

Metric	P&O-AT (%)	FLC (%)	PID (%)
Average CPU (%)	11.43	15.46	14.00
RAM Memory	90.57 MB	90.71 MB	91.20 MB

For all three controllers, the average RAM value was similar, around 90.8 MB.

According to the local server characteristics and the results in the table above, the computational expenditure for the 4 heliostats connected in parallel, with a sampling time of 1 second, is light and does not generate an impact on consumption.

On the other hand, during open-field experimental tests, a performance analysis of temperature at a target point was conducted for the three controllers, considering, for this case study, certain external load conditions specified by IEC 62817. These include: mean aerodynamic load (wind) generated on the structure, deflection and pointing error, turbulent fluid (dynamic wind) causing oscillations that degrade stationary loads, and mechanical oscillations (structural vibration) that degrade tracking precision and increase mechanical fatigue in components and joints. Figure 13 shows recorded values of global solar radiation, wind speed, and wind direction acquired during the experimental period from an INER meteorological system (code: 19455607) located on the south campus of the Universidad Politécnica Salesiana, Quito.

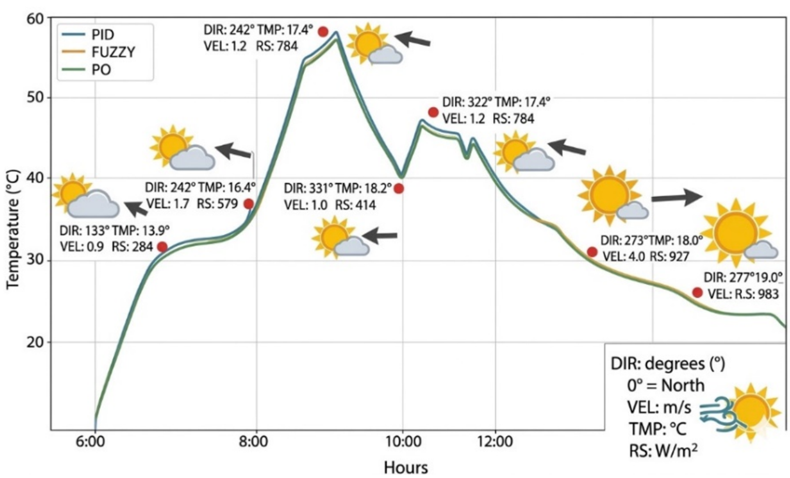

Fig. 13. Temporal evaluation of environmental variables and target temperature under PID, FLC, and P&O-AT control.

According to the figure above, the thermal profile shows variability during experimentation due to the maximum and minimum conditions of solar radiation (RS) and the influence of wind speed (VEL), which causes a relative increase in thermal losses due to convection [4]; that is, there are hours of the day when the thermal profile drops even with maximum radiation, due to increased wind dynamics.

Although the thermal profiles of the three controllers show similar behavior, the concentration at the target point for the PID controller maintains a favorable thermal difference, indicating greater thermal utilization under equal operating conditions, including execution time, wind speed and direction, solar radiation, ambient temperature, distance to the target vector, reflective material, sensors, and actuators.

4 Discussion

The premise of this research stems from the results of a systematic literature review on control systems for concentrating solar power (CSP) plants, the vast majority of which focus on implementing basic and advanced control algorithms on simulation platforms, neglecting experimental validation. Such validation is essential for evaluating real-world performance under non-ideal physical conditions, such as aerodynamic disturbances, mechanical friction, and structural vibrations.

The formal criteria for the documented state-of-the-art process include databases such as Scopus and ResearchGate, AI-based semantic search methods, and filtering by year. In this context, a deficit is identified in the analysis of results comparing the performance of robust or classical controllers implemented in physical systems. Consequently, this article contributes an analysis of the performance of classical controllers (PID, FLC, and P&O-AT) operating in a laboratory heliostat array under the same operating conditions.

The experimental validation of these algorithms is conducted under dynamic disturbance conditions and under specified external loads defined by the IEC 62817 standard, including mean aerodynamic load, turbulent fluid, and mechanical oscillations. In this regard, the IEC 62817 standard reinforces the interpretation of experimental results by linking the controller's performance to the structure's mechanical response during solar tracking. Thus, the thermal response observed at the target point depends not only on the control algorithm but also on the heliostat's ability to maintain accuracy under external loads, since small angular deviations in the azimuth and elevation axes can reduce the effective concentration of solar radiation, causing a variation in the thermal profiles.

This study provides relevant information on efficiency, the viability of low-cost computational options, and the complexity of implementation, highlighting the importance of considering results for scalability and available resources in limited implementation contexts.

The experimental results also reveal a trade-off among control robustness, thermal performance, and computational cost. Under equivalent operating conditions and external disturbances defined by the IEC 62817 criteria, the PID controller achieved a more balanced overall behavior in terms of tracking precision, stability, and thermal concentration at the target point. In contrast, the FLC demonstrated faster disturbance rejection and adaptive response capabilities, although at higher computational cost, while the P&O-AT approach favored low computational resource usage at the expense of slower convergence and reduced pointing precision. These findings suggest that controller selection in CSP applications should consider not only tracking accuracy but also hardware limitations, scalability requirements, and real-time implementation constraints.

During project execution, several difficulties arose in analyzing the azimuth angle (PID, FLC, and P&O-AT) due to sensor precision and stability issues caused by their low resolution. Instead, it should be noted that, being a laboratory CSP system, it is necessary to initially apply a manual calibration routine to fix the target vector for each heliostat [13]. Furthermore, as the number of heliostats increased, it became necessary to integrate a connection manager at the local server endpoint to avoid data packet saturation in the communication.

Due to the high costs of developing CSP at the experimental laboratory level, the use of low-cost sensors calibrated against a reference sensor [14] is recommended to provide adequate feedback on the physical phenomenon to the control system. Additionally, for non-invasive technological scaling of already implemented systems, the use of Industry 4.0 tools such as IoT, cloud computing, and data analytics is necessary for supervision, monitoring, and centralized control, especially when energy storage and additional subsystems are integrated [11, 15]. Moreover, given the research niche of this study, it is imperative to compare robust controllers for performance analysis under standardized norms for CSP use.

5 Conclusion

An analysis of the behavior of the controllers implemented in the CSP under equivalent conditions enabled a comparison of objective performance metrics, including precision, stability, convergence, computational efficiency, and thermal performance. The FLC stood out for maintaining stable tracking on both axes with a shorter settling time, but with increased error variation and overshoot. It demonstrated rapid correction against disturbances and external loads and effective convergence toward the setpoint, albeit at the cost of higher CPU consumption (15.46%) due to the inherent complexity of the inference and defuzzification processes. By contrast, the P&O-AT algorithm showed a longer settling time due to its iterative nature, exhibited more aggressive corrections during transients, and achieved lower precision relative to the reference, while demonstrating the lowest use of computational resources (11.43% CPU), favoring its application in embedded or low-power systems. The PID controller achieved a better overall balance between precision and stability on both axes, recording lower MAE/RMSE values and moderate overshoot, with intermediate CPU consumption (14%). In this regard, during experimental tests under equal operating conditions, thermal performance followed a similar trend under external loads (radiation, wind, etc.), generating convection losses; however, PID showed a thermal advantage at the target point, demonstrating better pointing and solar tracking. RAM consumption was similar in all cases (91 MB), underscoring the importance of considering computational cost when selecting the control algorithm in contexts where scalability and hardware integration have limited capacity.

References

1. A. Z. Hafez, A. M. Yousef, N. M. Harag, Solar tracking systems: Technologies and trackers drive types – A review. Renew. Sustain. Energy Rev., **91**, 754–782 (2018). https://doi.org/10.1016/j.rser.2018.03.094
2. F. Ordóñez, D. Vaca-Revelo, J. Lopez-Villada, Assessment of the Solar Resource in Andean Regions by Comparison between Satellite Estimation and Ground Measurements: Study Case of Ecuador. J. Sustain. Dev., **12**(4), 62 (2019). https://doi.org/10.5539/jsd.v12n4p62
3. C. Atkinson, C. Sansom, H. Almond, C. Shaw, Coatings for concentrating solar systems – A review. Renew. Sustain. Energy Rev., **45**, 113–122 (2015). https://doi.org/10.1016/j.rser.2015.01.015
4. J. Martínez-Nogales, J. Lara-Sinaluisa, N. Perugachi-Cahueñas, J. F. Moreno-Ayala, Estudio de la transferencia de calor en energías renovables: Optimización de paneles solares térmicos y sistemas geotérmicos. Pol. Con., **10**(6), 834–858 (2025). https://doi.org/10.23857/pc.v10i6.9678
5. R. F. Fuentes-Morales, A. Díaz-Ponce, M. I. Peña-Cruz, P. M. Rodrigo, L. M. Valentín-Coronado, F. Martell-Chavez, C. A. Pineda-Arellano, Control algorithms applied to active solar tracking systems: A review. Sol. Energy, **212**, 203–219 (2020). https://doi.org/10.1016/j.solener.2020.10.071
6. W. M. Hamanah, A. S. Salem, M. A. Abido, F. A. Al-Sulaiman, A. M. Qwbaiban, T. G. Habetler, Modeling, Implementing, and Evaluating of an Advanced Dual Axis Heliostat

Drive System. J. Sol. Energy Eng., **144**(4), 041001 (2022). https://doi.org/10.1115/1.4052958

7. Z. Zeng, D. Ni, G. Xiao, Real-time heliostat field aiming strategy optimization based on reinforcement learning. Appl. Energy, **307**, 118224 (2022). https://doi.org/10.1016/j.apenergy.2021.118224
8. J. A. Carballo, J. Bonilla, N. C. Cruz, J. Fernández-Reche, J. D. Álvarez Hervás, L. Valenzuela, M. Berenguel, Reinforcement learning for heliostat aiming: Improving the performance of Solar Tower plants. Appl. Energy, **377**, 124574 (2025). https://doi.org/10.1016/j.apenergy.2024.124574
9. I. Reda, A. Andreas, Solar Position Algorithm for Solar Radiation Applications. Sol. Energy, **76**(5), 577–589 (2004). https://doi.org/10.1016/j.solener.2003.12.003
10. R. Zhu, D. Ni, A model predictive control approach for heliostat field power regulation aiming strategy under varying cloud-shading conditions. Energies, **16**(7), 2997 (2023). https://doi.org/10.3390/en16072997
11. Q. Liu, Z. Dai, Y. Wei, D. Wang, Y. Xie, Transformative impacts of AI and wireless communication in CSP heliostat control systems. Energies, **18**(5), 1069 (2025). https://doi.org/10.3390/en18051069
12. G. Ferruzzi, C. Delcea, A. Barberi, V. Di Dio, M. Di Somma, P. Catrini, S. Guarino, F. Rossi, M. L. Parisi, A. Sinicropi, S. Longo, Concentrating Solar Power: The State of the Art, Research Gaps and Future Perspectives. Energies, **16**(24), 8082 (2023). https://doi.org/10.3390/en16248082
13. J. Sattler, M. Röger, P. Schwarzbözl, R. Buck, A. Macke, C. Raeder, J. Göttsche, Review of heliostat calibration and tracking control methods. Sol. Energy, **207**, 110–132 (2020). https://doi.org/10.1016/j.solener.2020.06.030
14. R. C. de Barros, J. M. S. Callegari, D. do C. Mendonça, W. C. S. Amorim, M. P. Silva, H. A. Pereira, Low-cost solar irradiance meter using LDR sensors, in Proceedings of the 13th IEEE International Conference on Industry Applications (INDUSCON), Sao Paulo, Brazil, 12-14 November, (2018). https://doi.org/10.1109/INDUSCON.2018.8627176
15. G. Chaudhary, J. J. Lamb, O. S. Burheim, B. Austbø, Review of Energy Storage and Energy Management System Control Strategies in Microgrids. Energies, **14**(16), 4929 (2021). https://doi.org/10.3390/en14164929